

# Aerodynamic Optimisation of Civil Aero-Engine Nacelles by Dimensionality Reduction and Multi-Fidelity Techniques

Fernando Tejero<sup>1\*</sup>, David G. MacManus<sup>1</sup>, Josep Hueso-Rebassa<sup>1</sup>,  
Francisco Sanchez-Moreno<sup>1</sup>, Ioannis Goulos<sup>1</sup> and Christopher Sheaf<sup>2</sup>

<sup>1</sup>*School of Aerospace, Transport and Manufacturing, Cranfield University, MK43 0AL,  
Bedfordshire, United Kingdom*

<sup>2</sup>*Rolls-Royce plc, DE24 8BJ, Derby, United Kingdom*

*\*Corresponding author: f.tejero@cranfield.ac.uk*

---

## Abstract

**Purpose** - Aerodynamic shape optimisation is complex due to the high dimensionality of the problem, the associated non-linearity and its large computational cost. These three aspects have an impact on the overall time of the design process. To overcome these challenges, this paper develops a method for transonic aerodynamic design with dimensionality reduction and multi-fidelity techniques.

**Design/methodology/approach** - The developed methodology is used for the optimisation of an installed civil ultra-high bypass ratio aero-engine nacelle. As such, the effects of airframe-engine integration are considered during the optimisation routine. The active subspace method is applied to reduce the dimensionality of the problem from 32 to 2 design variables with a database compiled with Euler CFD calculations. In the reduced dimensional space, a co-Kriging model is built to combine Euler lower-fidelity and RANS higher-fidelity CFD evaluations.

**Findings** - Relative to a baseline aero-engine nacelle derived from an isolated optimisation process, the proposed method yielded a non-axisymmetric nacelle configuration with an increment in net vehicle force of 0.65% of the nominal standard net thrust.

**Originality** - This work investigates the viability of CFD optimisation through a combination of dimensionality reduction and multi-fidelity method, and demonstrates that the developed methodology enables the optimisation of complex aerodynamic problems.

---

**Keywords:** Optimization, dimensionality reduction, multi-fidelity, active subspace, co-kriging

**Paper type:** Research paper

## **Nomenclature**

### **Abbreviations**

AV	Active Variable
BC	Boundary Condition
CFD	Computational Fluid Dynamics
CNPR	Core Nozzle Pressure Ratio
CRM	Common Research Model
CST	Class Shape Transformation
DoF	Degrees of Freedom
DSE	Design Space Exploration
FNPR	Fan Nozzle Pressure Ratio
GPF	Gross Propulsive Force
GTM	Generative Topographic Mapping
iCST	Intuitive Class Shape Transformation
LHS	Latin Hypercube Sampling
MFCR	Mass Flow Capture Ratio
NPF	Net Propulsive Force
NVF	Net Vehicle Force
RANS	Reynolds-Averaged Navier Stokes

### **Greek Symbols**

$\beta$	Boat-tail angle
$\psi$	Azimuthal angle

### **Roman Symbols**

$C$	Chord
$C_L$	Lift coefficient
$C_p$	Pressure coefficient
$D$	Nacelle drag
$f$	Non-dimensional factor

$F_N$	Net thrust
$L$	Length
$M$	Mach number
$r$	radius

**Subscripts**

$\infty$	Freestream
$DR$	Drag rise
$hi$	Highlight
$if$	Initial Forebody
$int$	Intake
$is$	Isentropic
$max$	Maximum radius
$nac$	Nacelle
$ref$	Reference
$sep$	Separation
$te$	Trailing Edge

**1. Introduction**

To meet the challenging performance targets defined by the Advisory Council for Aviation Research and Innovation in Europe (ACARE) in Flightpath 2050 (European Commission 2011), novel design and optimisation tools are required. In this respect, methods for quick aerodynamic shape optimisation will be fundamental to accelerate the overall aircraft design process and understand the feasibility of novel design concepts. Aerodynamic design can be specially demanding due to the large number of degrees of freedom considered, the non-linearity of the problem and the computational cost of the overall process (Skinner & Zare-Behtash 2018, Targui & Habashi 2022). For this reason emerging techniques such as dimensionality reduction or multi-fidelity methods are being considered.

A range of dimensionality reduction approaches have been successfully deployed in the past. Qiu et al. (2018) developed a framework that combined Proper Orthogonal Decomposition (POD) (Kim & Park 2021), to reduce the dimensional space, and a surrogate-based optimisation approach with a genetic algorithm. The method was deployed for the optimisation of the transonic RAE2822 airfoil and the transonic ONERA M6 wing. The number of design variables was reduced from 20 to 10 and from 42 to 20 for the airfoil and wing case studies, respectively. Relative to baseline geometries, the process yielded

optimal shapes with a drag reduction of about 13 drag counts and 34 drag counts, respectively. Viswanath et al. (2011) developed the generative topographic mapping (GTM) dimensionality reduction method, which is based on nonlinear latent variable models. It aims to transform a high-dimensional space into a low-dimensional latent space. Its capability for aerodynamic optimisation was tested with a transonic airfoil. The geometry was controlled with 30 design variables and the dimensionality was reduced to two dimensions after applying GTM. Within the reduced dimensional space an aerodynamic shape optimisation was carried out. The process provided a configuration with a drag increment of 8dc compared with a design from an optimisation in the full dimensional space. However, the GTM approach was 100 times less computationally expensive. Eivazi et al. (2020) investigated the capabilities of autoencoder networks for dimensionality reduction and feature extraction. Relative to other methods based on dynamic mode decomposition, it was found that the proposed approach was able to predict flow-fields with a higher accuracy. The active subspace (AS) technique (Constantine 2015) has been recently used for the design and optimisation of complex aerodynamic systems in which dimensionality reduction is required. It has been deployed for a wide range of applications such as airfoils (Grey & Constantine 2018), wings (Lukaczyk et al. 2014) or turbomachinery (Seshadri et al. 2018). Grey and Constantine (Grey & Constantine 2018) deployed the active subspace to guide the design of a transonic airfoil. The CST parametrisation was used and 10 design variables were employed to define the shape. It was found that the lift and drag could be represented with one and two active variables, respectively. As such, it was concluded that AS is an enabling method to accelerate the design process in a reduced dimensionality. Lukaczyk et al. (2014) used the active subspace method for the redesign of the ONERA M6-transonic wing. The aerodynamic shape was parametrised with 50 Free-Form Deformation (FFD) design variables. The relatively high-dimensional space was reduced to one and two active variables for the lift and drag, respectively. The process was used for a lift-constrained drag minimisation study. Relative to the baseline geometry, a new configuration with approximately 14% drag reduction was identified.

Another challenge of optimisations in high-dimensional spaces is that a large number of shapes are evaluated in the process (Xie et al. 2022). If the calculations are with higher-fidelity methods, the overall computational overhead may become prohibitive. For this reason, multi-fidelity methods have been used in the design of complex systems. Likeng et al. (2013) used a co-Kriging multi-fidelity approach for the design of a transonic wing-body configuration at mid-cruise conditions. The low-fidelity data was gathered with a full potential method and the high-fidelity samples were obtained with RANS CFD. The optimisation based on these multi-fidelity methods produced a configuration with a reduction of 16.5% drag coefficient relative to a reference shape. Zhang et al. (2021) developed a framework for aerodynamic shape optimisation with multi-fidelity deep neural network surrogate models. The data samples were gathered with RANS CFD evaluations in which the low- and high-fidelity were obtained with a coarse and fine mesh, respectively. The tool was deployed for the optimisation of the DLR-F4 wing-body configuration at transonic conditions. The process identified a configuration with an increase in  $C_L/C_D$  of 18.1% with respect to a baseline geometry.

Relative to conventional in-service aero-engines, it is expected that future civil archi-

tures will use higher bypass ratio to lower the specific thrust and increase the propulsive efficiency (Birch 2000, Xue et al. 2019). This may result in a larger fan diameter and size of the different housing components. If traditional design rules are applied, there will be an increase in the wetted area and therefore in the drag and overall weight. For this reason, it is envisaged that the next generation of aero-engines will use compact nacelle and exhaust systems to retain the benefits from the engine cycles (Daggett et al. 2003). These new configurations are also likely to be installed in close-coupled installation positions due to ground clearance and structural requirements. This can result in large installation penalties that could negate the expected cycle benefits. For this reason, the effect of installation position should be considered at an early stage of the design process because it may affect the feasibility of these new architectures. Previous studies have quantified the impact of powerplant integration on the overall aircraft performance for a wide range of installation positions. Sibili et al. (2012) investigated the integration of different propulsion systems for very high bypass ratio engines. It was found that across the different installation positions the mission fuel burn could vary up to 3.4%. Stankowski et al. (2017) assessed the effect of engine installation position, size and power settings on a typical 300-seater aircraft. For this investigation only engine positions forward of the wing leading edge were considered. Within the cruise segment, the engine with lower specific thrust had a 4.8% reduction in fuel burn with respect to a baseline architecture. Jing et al. (2013) carried out the optimisation of the nacelle/pylon position on a transonic aircraft. The overall drag was minimised while preserving the targeted lift coefficient of  $C_L = 0.5$ . The optimisation process was driven towards forward installation position which minimised the shock wave strength on the nacelle and pylon inboard side. The process resulted in a new shape with a reduction of 3.7dc with respect to the original configuration. Tejero, Goulos, MacManus & Sheaf (2020) investigated the effects of aircraft integration for forward and close-coupled installation positions. The study considered two different aero-engines configurations in which the nacelle length changed from  $L_{nac}/r_{hi} = 3.8$  to 3.1. The study highlighted that the short nacelle ( $L_{nac}/r_{hi}=3.1$ ), representative of a future civil aero-engine, had larger installation penalties than the conventional long nacelle ( $L_{nac}/r_{hi}=3.8$ ). For forward installation positions, the installation penalties were low and the benefits of the short nacelle that were quantified in isolation were realised. However, for a more closely-coupled installation the benefits reduced by a factor of about 3.

One of the key contributors to the overall net vehicle force of the aircraft configuration is the nacelle (Tejero, Goulos, MacManus & Sheaf 2020, Goulos et al. 2020). For this reason, it is required to understand its sensitivity for installed configurations. Although previous studies have considered nacelle design and optimisation for combined airframe-engine systems, the process was only driven by lower fidelity evaluations. Koc et al. (2005) optimised the DRL-F6 wing-body-nacelle-pylon configuration with an adjoint method using Euler calculations. Overall 82 design variables were used. Relative to a baseline configuration, the process provided design with 16dc reduction at the same lift coefficient. Smith et al. (2013) developed an adjoint optimisation framework for the design optimisation of a wing-body-nacelle-pylon. The routine was also driven by inviscid CFD evaluations in which a total of 159 design variables were considered. For the

optimised configuration a method to account for the viscous terms was used to predict the main aerodynamic characteristics of the integrated system. It was identified that the adverse flow features that manifest on the inboard side of the nacelle could be mitigated with the proposed method. It was concluded that until emerging methods for viscous-flow shape optimisation for complex and high-dimensional problems are developed, the proposed inviscid shape optimisation approach followed by viscous shape correction was sufficient to derive representative aerodynamic shapes.

Within the context of future compact civil aero-engine nacelles, there is a clear need for optimisations that are driven with information from higher CFD fidelities in which the effects of aircraft integration are considered. However this has not been previously performed due to the large computational cost associated to it. For this reason, it has been a common practice to carry out isolated nacelle optimisation studies and assess the coupled aerodynamic performance airframe-engine for the derived configurations. Nonetheless Ultra High Bypass Ratio (UHBPR) configurations are expected to be installed in close-coupled positions in which the aerodynamic coupling between both systems will increase. For this reason, enabling methods for the optimisation of installed configurations are required. The novelty of this paper is in the development of an optimisation method for high-dimensional design spaces. The developed approach is applied to design a compact aero-engine nacelle in which the effects of integration are considered during the optimisation. The investigated problem covers a relatively large dimensional space with more than 30 design variables. For this reason, a dimensionality reduction technique is used to accelerate the design process. A database of installed cases is generated using Euler CFD solutions as lower fidelity upon which the active subspace technique is employed. In the reduced design space, a range of RANS CFD calculations are performed and a multi-fidelity co-Kriging approach is used. Whilst the proposed method is used for aero-engine nacelle design applications, it can be applied for the optimisation of other complex aerodynamic problems (Millot et al. 2020, Embuena et al. 2018).

## **2. Methodology**

The developed numerical approach for the aerodynamic optimisation of installed turbofan engines extends previous work in the design of civil aero-engines (Tejero, Goulos, MacManus & Sheaf 2020, Goulos et al. 2020, Rebassa et al. 2020, Sanchez-Moreno et al. 2022). It has a parametric geometry definition capability based on intuitive Class Shape Transformation (iCST) functions (Christie et al. 2017) for the design of the nacelle (Tejero et al. 2021, Tejero, MacManus & Sheaf 2020), intake (Christie et al. 2019), exhaust (Goulos et al. 2018) and pylon (Goulos et al. 2020), and automatically creates the computational domain in which structured prism layer are used near the wall and tetrahedral elements are employed in the rest of mesh. Two different CFD fidelities can be used during the design process: Euler and RANS (*ANSYS FLUENT User's Guide* n.d.). A set of data-driven techniques guide the optimisation, which include dimensionality reduction (Constantine 2015), surrogate modelling and a multi-fidelity capability (Baykatar & Turalioglu 2005). The overall process is coupled with a thrust-drag bookkeeping method to evaluate the aerodynamic performance for the combined airframe-engine architectures

(Goulos et al. 2020).

This work uses the NASA CRM as a representative commercial transport aircraft (Vassberg et al. 2008, Vassberg & et al. 2014). The powerplant is integrated in the same spanwise location and with the same values of pitch and toe angles as the benchmark CRM nacelle throughflow configuration (Rivers & Dittberner 2011). Although this study mainly focuses in the optimisation of the aero-engine nacelle, the other housing components have been designed with established methods to alleviate any adverse flow features across the design space considered (Christie et al. 2019, Goulos et al. 2018, Tejero, Goulos, MacManus & Sheaf 2020). The pylon is built by vertically mounting a series of aerofoil sections (Goulos et al. 2020). The Turbomatch tool (Macmillan 1974) has been used to derive the engine cycle characteristics. It models the engine cycle to give the boundary conditions for the exhaust system and was also employed to calculate the bypass and nozzle areas.

The intake, nacelle, exhaust and pylon geometries are parametrised with iCST curves. The nacelle parametric representation uses 7 intuitive design variables to define a single 2D aero-line ( $r_{hi}, L_{nac}, r_{te}, r_{if}, f_{max}, r_{max}$  and  $\beta_{nac}$ ) (Figure 1). A series of iCST curves in the cylindrical coordinate system are used to define 3D non-axisymmetric aero-engine nacelles. The azimuthal variation of each 2D design variable is controlled at user-prescribed azimuthal angles (Tejero et al. 2021) which results in a 3D parametric definition of a drooped and scarfed non-axisymmetric aero-engine nacelle (Tejero et al. 2022). The general form of this iCST construction can be employed for fully asymmetric configurations (Figure 2). For this study 8 aero-lines are controlled in intervals of  $45^\circ$ . As such, for fixed droop angle, scarf angle,  $L_{nac}/r_{hi}$  and  $r_{te}/r_{hi}$  the full 3D geometry is controlled with 32 degrees of freedom. A detailed description of the iCST parametrisation has been provided by Tejero et al. (2021).

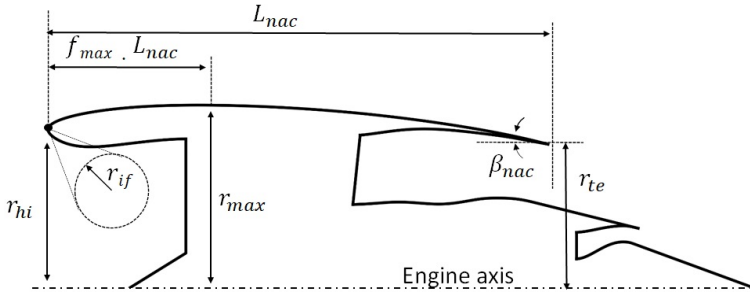


FIGURE 1: Design variables used to define the aero-engine nacelle

The developed method has a multi-fidelity capability to accelerate the overall design process. The higher-fidelity CFD data is generated from the viscous and compressible steady Favre-averaged Navier-Stokes equations (*ANSYS FLUENT User's Guide* n.d.) with the  $k-\omega$  SST turbulence closure (Menter 1994). The solver uses an implicit scheme and a density-based approach. The lower-fidelity CFD is based on compressible, inviscid Euler equations that are solved with a pressure-based algorithm (*ANSYS FLUENT User's Guide* n.d.). A Green-Gauss scheme and a second-order spatial discretization are used for

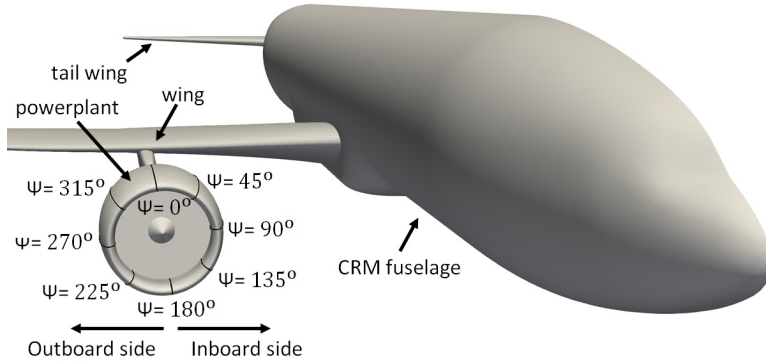


FIGURE 2: Powerplant integrated into the NASA CRM and aero-lines controlled to define the 3D non-axisymmetric nacelle

both fidelities. Kinetic theory is employed to compute the thermal conductivity and the Sutherland’s law is used to estimate the dynamic viscosity (Sutherland 1893). For both numerical approaches the aircraft is enclosed in a hemispherical domain located at 100 wing cords as per the guidelines from the 4<sup>th</sup> AIAA Drag Prediction Workshop (DPW) (Vassberg & et al. 2014). For the higher-fidelity CFD simulations the first layer height is adjusted to ensure a  $y^+$  below 1 along the full aircraft and the overall cell count is approximately 115 million cells. The numerical validation of the computational approach and mesh independence studies have been reported by Goulos et al. (2020). For the Euler calculations the boundary layer refinement in the normal direction is eliminated. In addition, the cell size on the wall in the parallel directions is increased by a factor of around 2. This resulted in an overall cell count of approximately 20 million which ensured a tractable capability for a comprehensive design space exploration with this fidelity.

The freestream conditions were set with pressure-farfield boundary condition (BC) in which the Mach number, the static pressure and the static temperature were specified at the hemispherical boundary. The intake massflow derived from the user-prescribed MF CR is controlled with a pressure-outlet condition. The bypass and core nozzle inlets are modelled with a pressure-inlet BC with the total pressure and total temperature obtained from the 0D engine cycle analysis (Macmillan 1974). A symmetry plane with half-model of the NASA CRM is used to reduce the overall computational overhead. Whilst non-slip wall are employed in the powerplant and airframe for the higher-fidelity method, inviscid walls are set for the Euler calculations.

### 2.1. Dimensionality reduction: Active subspace method

To collect data across the relatively high-dimensional space considered in this work with 32 design variables, a design space exploration (DSE) based on the computationally efficient Latin Hypercube Sampling (LHS) technique (Helton & Davis 2003) is used. The different configurations are evaluated with the lower-fidelity Euler CFD approach to generate an initial database. With the Euler data from the DSE, the active subspace method is used to reduce the dimensionality of the optimisation problem. It aims to find a set of



new variables which are a linear combination of the full design space and can model the system's output. The mathematical implementation of the active subspace method follows the original derivation proposed by Constantine et al. (2014). A brief description of the method is provided in this section.

A scalar output  $f$  is a function of a vector  $\mathbf{x}$  with  $n$  dimensions,  $f=f(\mathbf{x})$ . The  $n \times n$  matrix  $\mathbf{C}$ , which is the covariance of the gradient across the design space, can be expressed as follow (Eq. 1):

$$\mathbf{C} = E [\nabla f \nabla f^T] \quad (1)$$

where the gradient vector of  $\nabla f$  is defined as (Eq. 2):

$$\nabla f = \left[ \frac{\partial f}{\partial x_1}, \frac{\partial f}{\partial x_2}, \dots, \frac{\partial f}{\partial x_n} \right] \quad (2)$$

The matrix of covariance of the gradient across the space ( $\mathbf{C}$ ) can be approximated with the snapshot method by using  $M$  samples (Eq. 3):

$$\mathbf{C} \approx \frac{1}{M} \sum_{n=1}^M \nabla f_i \nabla f_i^T \quad (3)$$

in which  $\nabla f_i$  is the gradient vector of the  $i$  sample (Eq. 4):

$$\nabla f_i = \nabla f x_i \quad (4)$$

Having approximated the matrix  $\mathbf{C}$ , an eigenvalue decomposition can be carried out (Eq. 5):

$$\mathbf{C} = \mathbf{W} \mathbf{\Lambda} \mathbf{W}^T \quad (5)$$

where  $\mathbf{W}$  is the matrix of eigenvectors and  $\mathbf{\Lambda}$  is a diagonal matrix with the eigenvalues. The values found in  $\mathbf{\Lambda}$  are in descending order and contain the energy modes of the identified active subspace directions. Then, the matrix of the active subspace  $\mathbf{U}$  can be built. For example, the first column of  $\mathbf{U}$  can be described as (Eq. 6):

$$U_1 = [w_{1,1}, w_{2,1}, w_{3,1}, \dots, w_{n,1}] \quad (6)$$

where  $w_{1\dots n,1}$  refers to active variable weights from the first column of the matrix  $\mathbf{W}$ .

To link the vector at the reduced dimensional space ( $\mathbf{x}_{as}$ ) with the vector of the original space ( $\mathbf{x}$ ), the matrix of the active subspace ( $U$ ) is used (Eq. 7):

$$\mathbf{x} = U \mathbf{x}_{as} \quad (7)$$

## 2.2. Multi-fidelity: co-Kriging

Co-Kriging is the extension of the Gaussian Process Regression (Kriging) method (Baykatar & Turalioglu 2005, Gong & Ma 2019) for multi-fidelity data. While Kriging methods rely on a single database of the same fidelity, co-Kriging utilises two sources of data with different fidelities to improve the prediction on the higher one. These usually

consist of a large and computationally efficient lower-fidelity (LF) dataset (labelled as 2) that is combined with a reduced and more expensive higher-fidelity (HF) database (labelled as 1). The objective of co-Kriging is to model the correlation between HF and LF data to predict the HF function at a reduced computational cost.

The co-Kriging implementation used in this study is based on the work developed by Han et al. (2010, 2012) and only a summary of the mathematical model is presented. As with many other response surface models (RSMs), co-Kriging uses a training and prediction step. In the training process the hyper-parameters of the statistical model are calculated to represent known data (training dataset), while during the prediction phase the model evaluates the function at the higher-fidelity model.

In matrix notation, the multi-fidelity prediction function ( $\hat{y}_1$ ) is dependent on the inverse of the correlation matrix ( $R^{-1}$ ) and the matrices  $\phi$ ,  $\beta$ ,  $y_s$  and  $F$  (Han et al. 2010, 2012) that are fitted during the training process (Eq. 8).

$$\hat{y}_1 = \phi^T \beta + r^T(x) R^{-1} (y_s - F \beta) \quad (8)$$

The correlation matrix ( $R$ ) models the correlation between data of the same fidelity ( $R_{11}$  and  $R_{22}$ ) as well as the correlation between different fidelities ( $R_{12}$ ,  $R_{21}$ ) (Eq. 9).  $R_{ij}$  are assumed to be dependent on the distance between two data points ( $x - w$ ) and modelled as a product series of correlation functions ( $R_k(\theta_{ij}^k, x_i^k - w_j^k)$ ) across the dimensionality of the problem ( $n$ ) (Eq. 10).

$$R = \begin{pmatrix} R_{11} & R_{12} \\ R_{21} & R_{22} \end{pmatrix} \quad (9)$$

$$R_{ij}(\theta_{ij}, x_i, w_j) = \prod_{k=1}^n R_k(\theta_{ij}^k, x_i^k - w_j^k) \quad (10)$$

where  $\theta_{ij}^k$  are the distance weights, which correspond to the key hyper-parameters to be tuned in the training step,  $k$  indicates each of the dimensions of the problem ( $0 \leq k \leq n$ ) and implies that there will be  $n$  weight parameters for each combination of  $i$  and  $j$ .

Within this work, a Gaussian correlation function is considered (Eq. 11).

$$R_k(\theta, x - w) = e^{-\theta(x-w)^2} \quad (11)$$

The values of the hyper-parameters are obtained through the maximisation of the logarithmic likelihood function ( $\ln(L(\theta_{11}, \theta_{22}, \theta_{12}))$ ) (Eq. 12). The maximisation of this function is conducted with a Genetic Algorithm (GA) optimisation method (Tonda 2019). The implementation of the co-Kriging methodology used in this investigation has been validated with benchmark functions (Rebassa et al. 2020).

$$\ln(L(\theta_{11}, \theta_{22}, \theta_{12})) = \frac{1}{2} ((s_1 + s_2) \ln(\sigma_1^2) + \ln(|R|)) \quad (12)$$

where  $s_1$  and  $s_2$  correspond to the number of high- and low-fidelity training data samples respectively and  $\sigma_1^2$  refers to the process variance.

Operating conditions	Value
Mach number	0.85
altitude	10668m
MFCR	0.7
FNPR	2.2
CNPR	1.5

TABLE 1  
Summary of engine cycle and operating conditions

### 3. Results and analysis

The installed nacelle aerodynamic shape optimisation is conducted for mid-cruise conditions with  $M = 0.85$  and the CRM designed lift coefficient of  $C_L = 0.5$  (Vassberg et al. 2008, Vassberg & et al. 2014). The aero-engine operates with a bypass ratio larger than 15, which is expected for large turbofans (Epstein 2014), and a nominal standard net thrust ( $F_N$ ) of approximately 60kN (Goulos et al. 2016). The values of FNPR and CNPR were estimated to minimise the specific fuel consumption at design point (Goulos et al. 2018). The intake was sized to ensure a mass flow capture ratio of  $MFCR = 0.7$  (Tejero et al. 2019). A summary of the engine cycle and operating conditions is presented in Table 1. This study considers a compact aero-engine nacelle with  $L_{nac}/r_{hi} = 3.1$  (Tejero et al. 2021).

The numerical analysis and optimisation is performed for an installation position that is expected for future civil aero-engines. The powerplant is placed in the same wing spanwise location as the NASA CRM throughflow configuration. The installation position is defined as an axial ( $d_x$ ) and vertical ( $d_z$ ) offset between the nacelle top-line trailing edge and the wing leading edge (Tejero, Goulos, MacManus & Sheaf 2020). For this study, the normalised axial offset was  $d_x/C_{wing}=0.0$  and the normalised vertical offset was set to  $d_z/C_{wing}=0.1$ , where  $C_{wing}$  is the mean chord wing. The metric that is used to drive the optimisation is the net vehicle force (NVF) (Eq. 13), for which its value is maximised during the process. It was derived by Goulos *et al.* (Goulos et al. 2020) as a thrust drag bookkeeping method to account for the aerodynamic performance of combined engines-architectures (Goulos et al. 2020, Tejero, Goulos, MacManus & Sheaf 2020).

$$NVF = NPF - D_{A/F} \quad (13)$$

where  $NPF$  is the powerplant net propulsive force in the drag domain and  $D_{A/F}$  refers to the airframe drag. The net propulsive force (NPF) can be decomposed into Eq. 14:

$$NPF = GPF^* - F_{G,0} - D_{nac}^* \quad (14)$$

where  $GPF^*$  is the installed modified gross propulsive force,  $F_{G,0}$  refers to the gauge stream force upstream at infinity and  $D_{nac}^*$  is the modified nacelle drag (Goulos et al. 2020, Tejero, Goulos, MacManus & Sheaf 2020).

The design and optimisation process of the installed aero-engine nacelle starts with a design space exploration based on a Latin Hypercube Sampling (LHS) (Helton & Davis 2003) at the high dimensional space, i.e. 32 nacelle design variables. Overall, approximately 800 non-axisymmetric nacelle configurations were evaluated with the lower-fidelity CFD approach. This provides a ratio of  $N_{samples}/N_{DoF} \approx 25$ . The active subspace method was used (Section 2.1) and for the performance metric of interest, i.e. NVF, it was found that there was a reduction of one order of magnitude in the eigenvalues with the first two active subspace vectors. Similar threshold has been successfully used for aerodynamic applications in the open literature (Li et al. 2019). As such, the dataset can be projected in two active variables (AV) to easily identify optimal parts of the design space in the reduced dimensionality (Figure 3). It can be observed that the active variable AV1 has a larger influence on NVF across the space than AV2.

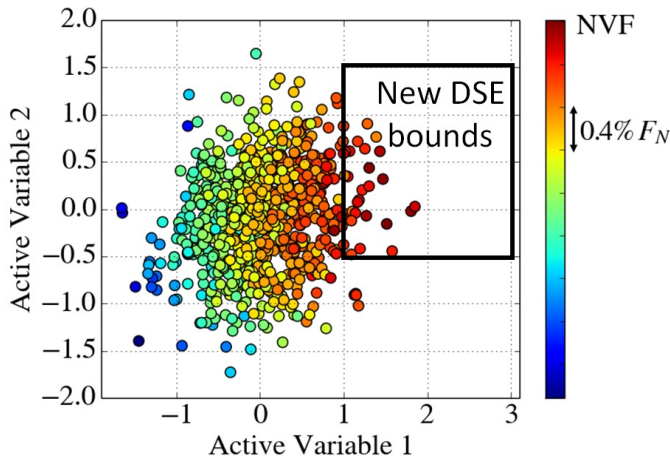


FIGURE 3: Projection of the 32 dimensional space into 2 after applying the active subspace method. The bounds of the new refined DSE are also marked

The weights ( $w_i$ ) of the active variables (Eq. 6) can be also used to identify which nacelle variables have a leading impact on the NVF metric. Figure 4 presents the  $w_i$  for the azimuthal aero-lines of  $\psi = 0^\circ, 45^\circ, 90^\circ, 135^\circ$  and  $180^\circ$ . They are the aero-lines that define the inboard side of the aero-engine nacelle (Figure 2), which is expected to have a larger contribution into the net vehicle force for the installed configuration (Tejero, Goulos, MacManus & Sheaf 2020). For the first AS vector, the greatest weights appear for  $r_{max}$  at the top-line ( $\psi = 0^\circ$ ) and in-board side-line ( $\psi = 90^\circ$ ), and for  $\beta_{nac}$  at the inboard side-line. Previous nacelle studies for isolated configurations have highlighted the large impact on nacelle drag of the maximum radius at the top-line due to the strong shock waves that appear on it (Tejero, MacManus & Sheaf 2020). The active subspace weights highlight that the inboard side-line ( $\psi = 90^\circ$ ) is an important driver for the aerodynamic performance of the aircraft-powerplant configuration. This can be explained by the effect that both variables ( $r_{max}$  and  $\beta_{nac}$ ) can have on the distance between the inboard side of the nacelle and the airframe, which has an impact on the overall NVF

performance (Goulos et al. 2020). It is also worth highlighting that  $\beta_{nac}$  at  $\psi = 45^\circ$  has a considerable weight on AV1. This variable can be used to control the distance between the powerplant and the wing and, therefore, has an impact on NVF. Conversely, different trends are obtained for the weights from AV2. However, this active variable has a smaller impact on NVF (Figure 3) and its relative effect on NVF with respect to AV1 is reduced.

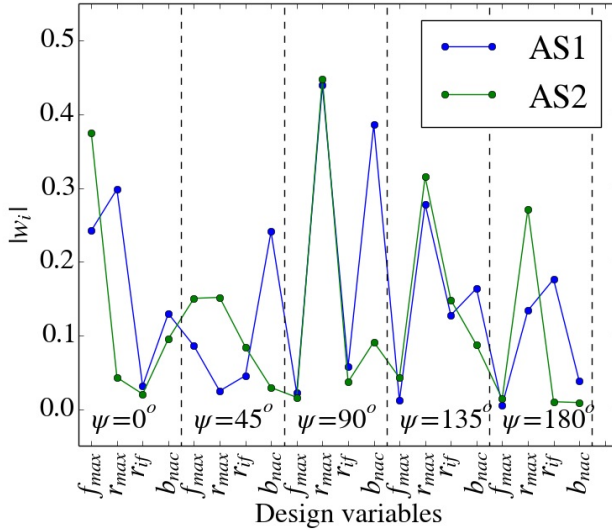


FIGURE 4: Weights of the 2 first active variables for the aero-lines that define the nacelle inboard side

Having identified potential regions of maximum NVF in the active subspace (Figure 3), a new design space exploration was performed in the reduced dimensional space (Figure 5). In this case, a full factorial of 5x5 was performed and it covered the range between [1.0 and 3.0] in AV1 and [-0.5,1.5] in AV2, as shown in Figure 3. All the 25 non-axisymmetric nacelles were evaluated with Euler computations and a subset of 13 were assessed with the higher-fidelity RANS method (Figure 5).

The 25 CFD evaluations with the lower-fidelity model resulted in the identification of an initial optimal configuration derived from the Euler calculations. The design was located at  $AV1 \approx 1.75$  and  $AV2 \approx 0.6$  (Figure 6). This location is based on Euler calculations and the active subspace method. To account for the relative changes across the design space between fidelities, i.e Euler and RANS, the subset of 13 CFD simulations were used to generate a co-Kriging (Baykatar & Turalioglu 2005) multi-fidelity model (Section 2.2) in the reduced dimensional space. This resulted in a slight change of the optimal part of the design space with  $AV1 \approx 2.3$  and  $AV2 \approx 0.25$ . This new location is predicted by combining both the dimensionality reduction and multi-fidelity techniques. This optimum has a benefit of approximately  $0.075\%F_N$  with respect to the optimal position identified by only using the dimensionality reduction method (Figure 6), i.e. the design at  $AV1 \approx 1.75$  and  $AV2 \approx 0.6$ .

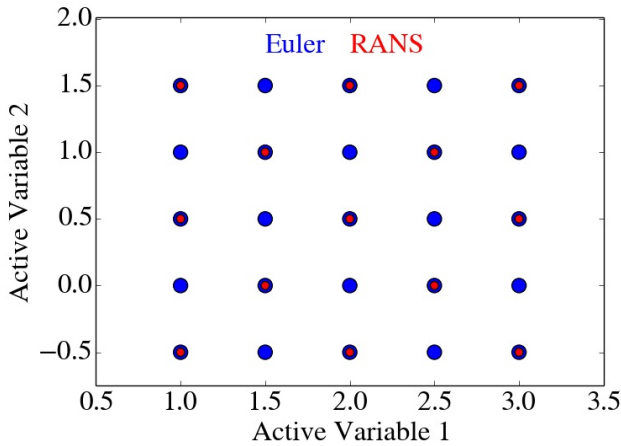


FIGURE 5: Refined design space exploration after applying the active subspace method

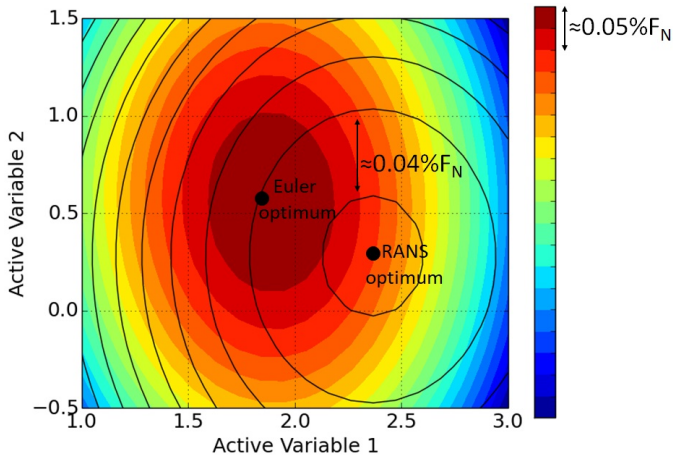


FIGURE 6: Refined design space exploration. Contour map refers to the Euler prediction and the lines are iso-lines of the predictions from the co-Kriging multi-fidelity model

To quantify the aerodynamic benefits of designing the aero-engine nacelle with the developed approach, its aerodynamic performance was compared with a baseline powerplant. This study uses as reference geometry a 3D non-axisymmetric aero-engine nacelle derived from an isolated optimisation with the tool developed by Tejero et al. (2019), Schreiner et al. (2020). Having obtained the powerplant from the isolated optimisation process, it was installed in the same installation position, i.e. normalised axial offset of  $d_x/C_{wing}=0.0$  and vertical offset of  $d_z/C_{wing}=0.1$ . The NVF changes between both architectures (optimised isolated and optimised installed) were compared at the higher-fidelity computational method of RANS. Relative to the baseline architecture, the installed optimisation yielded an optimal configuration with an improvement in net vehicle force

(NVF) of 0.65% of the nominal standard net thrust ( $F_N$ ).

To provide a better insight of the underlying mechanisms for the enhancement obtained with the combined dimensionality reduction and multi-fidelity methods, the constituent metrics of NVF have been analysed (Eq. 13). The normalised difference in the performance metrics between the nacelle from the developed method and the baseline geometry is presented in Figure 7. For the nacelle obtained from the developed method there is a benefit on  $NPF$  by  $1.05\%F_N$  which arises from changes to both the modified gross propulsive force and nacelle drag (Eq. 14). Although the new installed optimal geometry has a benefit of  $2.18\%F_N$  on  $D_{nac}^*$ , there is a penalty on modified gross propulsive force of about  $1.13\%F_N$ . Relative to the baseline installed architecture, the new configuration has a penalty of airframe drag of  $0.4\%F_N$  (Figure 7).

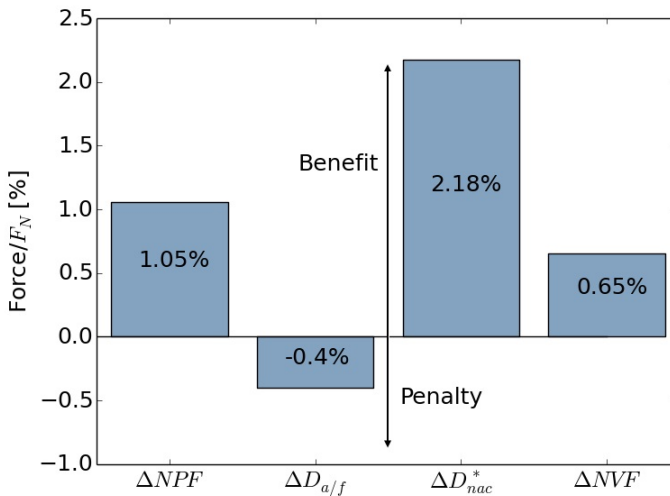


FIGURE 7: Breakdown of normalised forces. Difference between the installed optimised nacelle obtained with the developed method and the baseline configuration

The changes on the installed performance metrics ( $NVF$ ,  $NPF$ ,  $GPF^*$  and  $D_{nac}^*$ ) are accompanied by significant differences in the flow topology on the nacelle. Previous studies (Tejero, Goulos, MacManus & Sheaf 2020, Goulos et al. 2020) have identified adverse flow features on the aft end of the fangcowl inboard-side. This was caused by the reduced distances between the nacelle and the wing as well as the airframe. It resulted in a large flow acceleration near the trailing edge that terminated with strong shock waves which had an adverse impact on the overall installed performance (NVF). The same flow characteristics have been identified for the baseline geometry for which there is an initial acceleration around the nacelle lip which terminates in a shock wave and then the flow accelerates again to supersonic conditions and terminates in a second shock near the trailing edge (Figure 8a). The method developed in this study resulted in a nacelle design that alleviates this flow features (Figure 8b). For this reason there is a benefit of  $2.18\%F_N$  in the modified nacelle drag ( $D_{nac}^*$ ). It highlights the importance of installed design and

optimisation for future civil aero-engine configurations.

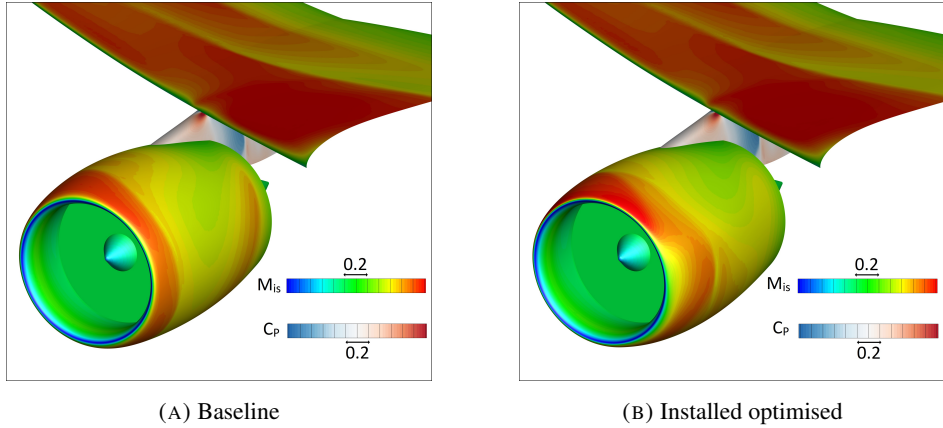


FIGURE 8: Flowfield characteristics on the nacelle inboard side and the CRM wing suction side

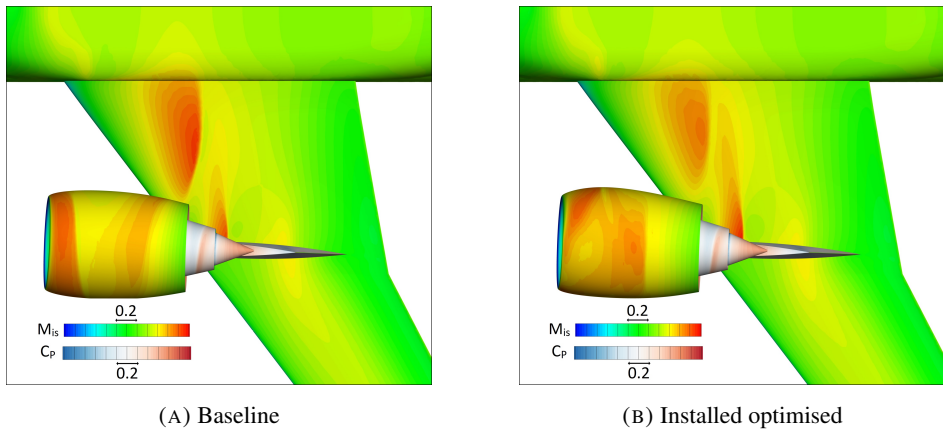


FIGURE 9: Flowfield characteristics on the bottom of the aero-engine nacelle and the CRM wing pressure side

There are also differences on the bottom side of the nacelle and the pressure side of the wing (Figure 9). For the baseline geometry there is a shock wave at the nacelle forebody and a second shock at the fancowl aft end (Figure 9a). The installed optimised configuration presents a more gradual initial flow acceleration around the nacelle lip with a single shock structure after the nacelle crest (Figure 9b). The powerplant integration has also a direct impact in the flow characteristics of the wing pressure side. When the new nacelle configuration obtained with the develop method is installed, there is a more gradual acceleration of the flow around the wing leading edge which terminates with a weaker shock than the baseline case. This controlled acceleration results in an increment of the static pressure on the wing forebody and produces a pressure drag penalty. This



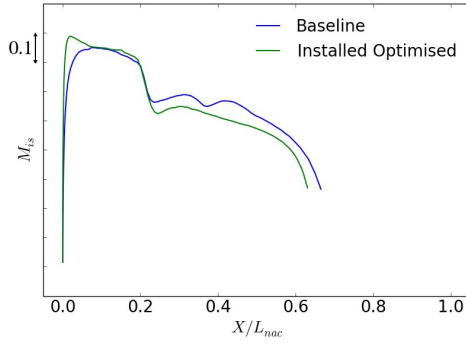
results in an airframe drag ( $D_{a/f}$ ) penalty of  $0.4\%F_N$  (Figure 7).

For the aero-lines with a larger impact on the  $NVF$  (Figure 4), the isentropic Mach number ( $M_{is}$ ) distribution between both nacelles is compared to provide a better insight of the flow characteristics (Figure 10). For the top-line ( $\psi = 0^\circ$ ) both architectures have similar flow topology with the same pre-shock  $M_{is}$  and shock location at  $X/L_{nac} \approx 0.2$ . The main difference arises in the initial acceleration on the nacelle lip which results in an increment of about 0.07 on the peak  $M_{is}$  for the installed optimised geometry (Figure 10a). A similar change was identified in the top-control line ( $\psi = 45^\circ$ ). For this aero-line the impact of aircraft integration manifests with a flow acceleration at the fancowl aft end (Figure 10b). This effect is more pronounced in the side line ( $\psi = 90^\circ$ ) in which for the baseline configuration there is a noticeable acceleration along the nacelle afterbody with a peak  $M_{is}$  located at  $X/L_{nac} \approx 0.8$ . At the same axial location, there is a reduction of  $M_{is} \approx 0.15$  for the installed optimised aero-engine (Figure 10c). For this aero-line ( $\psi = 90^\circ$ ) there are also differences in the nacelle forebody flow characteristics. Whilst the baseline has an initial large acceleration around the lip which terminated with a shock wave at  $X/L_{nac} \approx 0.15$ , the installed optimised configuration has a gradual acceleration in the first 25% of the nacelle length to terminate in a shock wave with similar pre-shock  $M_{is}$  of the baseline (Figure 10c). For the inboard bottom-control aero-line ( $\psi = 135^\circ$ ) of the baseline configuration there is an initial acceleration around the nacelle forebody that terminates with a shock at  $X/L_{nac} \approx 0.18$ . Then the flow reaccelerates up to  $X/L_{nac} \approx 0.75$  to decelerate towards the trailing edge. Conversely, the installed optimised architecture has a more controlled acceleration around the nacelle lip that terminates with a similar peak  $M_{is}$  as the reference configuration. After the axial location where the peak  $M_{is}$  is encountered, the installed optimal configuration has a smooth deacceleration along the nacelle aero-line (Figure 10d).

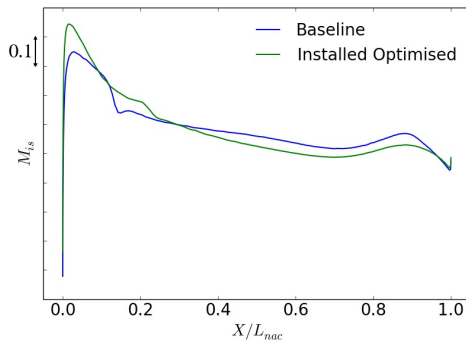
## 4. Conclusions

This article has described a novel approach for the optimisation of complex high dimensional problems. It addresses the viability of CFD optimisation through a combination of the active subspace dimensionality reduction technique and the co-Kriging multi-fidelity method.

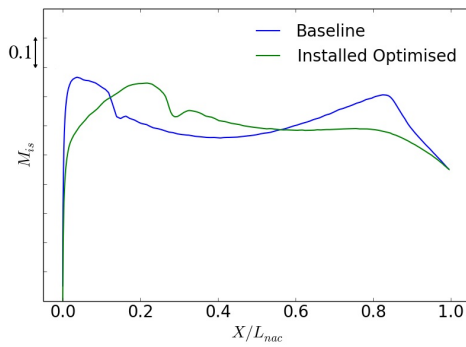
The approach has been used for the design and optimisation of an installed aero-engine nacelle. Overall, the method has enabled the successful redesign of a 32 degrees of freedom problem. The active subspace method was deployed to reduce the dimensionality from 32 to 2 design variables. The co-Kriging approach was used in the reduced dimensional space to link Euler evaluations with higher-fidelity RANS calculations. Relative to a baseline obtained with a current state-of-the-art nacelle design approach, the overall process yielded a new configuration with an increment in net vehicle force of 0.65% of the nominal standard net thrust. This was achieved by mitigating the adverse flow features that manifest on the aft end of the aero-engine nacelle inboard side. The developed capability is an enabling method for the design of complex aerodynamic systems.



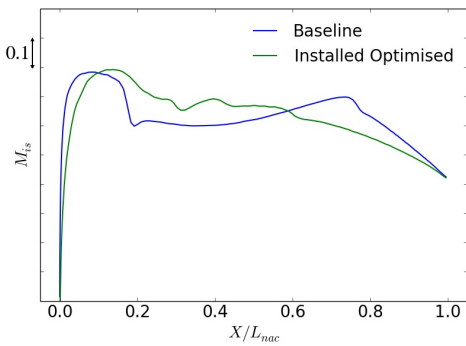
(A) Top line ( $\psi = 0^\circ$ )



(B) Inboard top-control line ( $\psi = 45^\circ$ )



(C) Inboard side line ( $\psi = 90^\circ$ )



(D) Inboard bottom-control line ( $\psi = 135^\circ$ )

FIGURE 10:  $M_{is}$  comparison for selected nacelle aero-lines

## Acknowledgments

This project has received funding from the Clean Sky 2 Joint Undertaking under the European Union's Horizon 2020 Research and Innovation Program under Grant Agreement No 820997.



## References

- ANSYS FLUENT User's Guide* (n.d.), 275 Technology Drive, Canonsburg, PA 15317.
- Baykatar, H. & Turalioglu, F. (2005), 'A kriging-based approach for locating a sampling site in the assessment of air quality', *Stochastic Environmental Research and Risk Assessment* **19**(5), 301–305.
- Birch, N. (2000), '2020 Vision: The Prospects for Large Civil Aircraft Propulsion', *The Aeronautical Journal* **104** (1038), 347–352.
- Christie, R., Heidebrecht, A. & MacManus, D. G. (2017), 'An Automated Approach to Nacelle Parameterisation Using Intuitive Class Shape Transformation Curves', *Journal of Engineering for Gas Turbines and Power* **139**(6), 062601–1 – 062601–9.
- Christie, R., Robinson, M., Tejero, F. & MacManus, D. (2019), 'The Use of Hybrid Intuitive Class Shape Transformation Curves in Aerodynamic Design', *Aerospace Science and Technology* **95**, 105473.
- Constantine, P. (2015), *Active Subspaces: Emerging Ideas for Dimension Reduction in Parameter Studies*, Society for Industrial and Applied Mathematics.
- Constantine, P., Dow, E. & Qiang, Q. (2014), 'Active subspace methods in theory and practice: Applications to kriging surfaces', *SIAM Journal on Scientific Computing* **36**(4), 1500–1524.
- Daggett, D., Brown, S. & Kawat, R. (2003), Ultra-Efficient Engine Diameter Study, Technical Report CR-2003-212309, NASA.
- Eivazi, H., Veisi, H., Naderi, M. & Esfahanian, V. (2020), 'Deep neural networks for nonlinear model order reduction of unsteady flows', *Physics of Fluids* **32**.
- Embuena, F. T., Doerffer, P., Flaszynski, P. & Szulc, O. (2018), 'Passive Flow Control Application for Rotorcraft in Transonic Conditions', *International Journal of Numerical Methods for Heat & Fluid Flow* **28**(5), 1080–1095.

- Epstein, A. (2014), ‘Aeropropulsion for Commercial Aviation in the Twenty-First Century and Research Directions Needed’, *AIAA journal* **52**(5), 901–911.
- European Commission (2011), Flightpath 2050: Europe’s Vision for Aviation, Technical Report ISBN 978-92-79-19724-6, Publications Office of the European Union.
- Gong, C. & Ma, B. (2019), ‘Shape Optimization and Sensitivity Analysis of a Morphing-Wing Aircraft’, *International Journal of Aeronautical and Space Sciences* **20**, 57–69.
- Goulos, I., Otter, J., Tejero, F., Rebassa, J. H. & MacManus, D. (2020), ‘Civil Turbofan Propulsion Aerodynamics: Thrust-Drag Accounting and Impact of Engine Installation Position’, *Aerospace Science and Technology* **111**, 106533.
- Goulos, I., Stankowski, T., MacManus, D., Woodrow, P. & Sheaf, C. (2018), ‘Civil Turbofan Engine Exhaust Aerodynamics: Impact of Bypass Nozzle After-Body Design’, *Aerospace Science and Technology* **73**, 85–95.
- Goulos, I., Stankowski, T., Otter, J., MacManus, D., Grech, N. & Sheaf, C. (2016), ‘Aerodynamic Design of Separate-Jet Exhausts for Future Civil Aero-Engine, Part 1: Parametric Geometry Definition and CFD Approach’, *Journal of Engineering for Gas Turbines and Power* **138**(8).
- Grey, Z. & Constantine, P. (2018), ‘Active Subspaces of Airfoil Shape Parameterizations’, *AIAA Journal* **56**(5), 2003–2017.
- Han, Z., Zimmermann, R. & Gortz, S. (2010), ‘A new cokriging method for variable-fidelity surrogate modeling of aerodynamic data, aiaa paper 2010-1225’, *48th AIAA Aerospace Science Meeting, Orlando, Florida*.
- Han, Z., Zimmermann, R. & Gortz, S. (2012), ‘Alternative cokriging model for variable-fidelity surrogate modeling’, *AIAA Journal Technical Notes* **50**(5), 1205–1210.
- Helton, J. C. & Davis, F. J. (2003), ‘Latin Hypercube Sampling and the Propagation of Uncertainty in Analyses of Complex Systems’, *Engineering and System Safety* **81**, 23–69.
- Jing, L., Zhenghong, G., Jiangtao, H. & Ke, Z. (2013), ‘Aerodynamic Design Optimization of Nacelle Pylon Position on an Aircraft’, *Chinese Journal of Aeronautics*.
- Kim, Y. & Park, C. (2021), ‘Multi-disciplinary Optimization of Wing Sandwich Structure using Proper Orthogonal Decomposition and Automatic Machine Learning’, *International Journal of Aeronautical and Space Sciences*.
- Koc, S., Kim, H. & Nakahashi, K. (2005), Aerodynamic Design of Wing-Body-Nacelle-Pylon Configuration, in ‘17th AIAA Computational Fluid Dynamics Conference, AIAA Paper 2005-4856’.
- Li, J., Cai, J. & Qu, K. (2019), ‘Surrogate-Based Aerodynamic Shape Optimization with the Active Subspace Method’, *Structural and Multidisciplinary Optimization* **59**, 403–419.

- Likeng, H., Zhenghong, G. & Dehu, Z. (2013), 'Research on Multi-Fidelity Aerodynamic Optimization Methods', *Chinese Journal of Aeronautics* **26**(2), 279–286.
- Lukaczyk, T., Constantine, P., Palacios, F. & Alonso, J. (2014), Active Subspaces for Shape Optimization, in '10th AIAA Multidisciplinary Design Optimization Conference, AIAA Paper 2014-1171'.
- Macmillan, W. (1974), Development of a Module Type Computer Program for the Calculation of Gas Turbine Off Design Performance, PhD thesis, Department of Power and Propulsion, Cranfield University, Cranfield University.
- Menter, F. R. (1994), 'Two-Equation Eddy-Viscosity Turbulence Models for Engineering Applications', *AIAA Journal* **32**(8), 1598–1605.
- Millot, G., Scholz, O., Ouhamou, S., Becquet, M. & Magnabal, S. (2020), 'Development of a 3D CFD Aerodynamic Optimization Tool and Application to Engine Air Intake Design', *International Journal of Numerical Methods for Heat & Fluid Flow* **30**(9), 4219–4239.
- Qiu, Y., Bai, J., Liu, N. & Wang, C. (2018), 'Global Aerodynamic Design Optimization Based on Data Dimensionality Reduction', *Chinese Journal of Aeronautics* **31**(4), 643–659.
- Rebassa, J. H., Tejero, F., Otter, J., Goulos, I. & MacManus, D. (2020), Multi-fidelity Assessment of Exhaust Systems for Complete Engine-Airframe Integrations, in 'Aerospace Europe Conference 2020'.
- Rivers, M. B. & Dittberner, A. (2011), Experimental Investigations of the NASA Common Research Model in the NASA Langley National Transonic Facility and NASA Ames 11-Ft Transonic Wind Tunnel (Invited), in '49th AIAA Aerospace Sciences Meeting including the New Horizons Forum and Aerospace Exposition, AIAA Paper 2011-1126'.
- Sanchez-Moreno, F., MacManus, D., Tejero, F., J.Matesanz-Garcia & Sheaf, C. (2022), Robustness of Optimisation Algorithms for Transonic Aerodynamic Design, in 'Proceedings of 9th European Conference for Aeronautics and Space Sciences, EUCASS-3AF'.
- Schreiner, B. D. J., Tejero, F., MacManus, D. & Sheaf, C. (2020), Robust aerodynamic design of nacelles for future civil aero-engines, in 'Proceedings of ASME Turbo Expo 2020: Turbomachinery Technical Conference and Exposition, GT2020-14470'.
- Seshadri, P., Shahpar, S., Constantine, P., Parks, G. & Adams, M. (2018), 'Turbomachinery Active Subspace Performance Maps', *Journal of Turbomachinery* **140**(4).
- Sibili, T., Savill, M., Sethi, V., MacManus, D. & Rolt, A. (2012), Numerical Simulation of Propulsion System Integration for Very High Bypass Ratio Engines, in 'Proceedings of ASME Turbo Expo 2012, GT2012-68908'.

- Skinner, S. & Zare-Behtash, H. (2018), ‘State-of-the-art in Aerodynamic Shape Optimisation Methods’, *Applied Soft Computing* **62**, 933–962.
- Smith, S., Nemeč, M. & Krist, S. (2013), Integrated Nacelle-Wing Shape Optimization for an Ultra- High Bypass Fanjet Installation on a Single-Aisle Transport Configuration, in ‘51st AIAA Aerospace Sciences Meeting Including the New Horizons Forum and Aerospace Exposition, AIAA Paper 2013-0543’.
- Stankowski, T., MacManus, D., Robinson, M. & Sheaf, C. (2017), ‘Aerodynamic Effects of Propulsion Integration for High Bypass Ratio Engines’, *Journal of Aircraft* **54**(6), 2017.
- Sutherland, W. (1893), ‘The Viscosity of Gases and Molecular Force’, *Philosophical Magazine* **5**(35), 507–531.
- Targui, A. & Habashi, W. (2022), ‘On A Reduced-Order Model-Based Optimization of Rotor Electro-Thermal Anti-Icing Systems’, *International Journal of Numerical Methods for Heat & Fluid Flow* **32**(8), 2885–2913.
- Tejero, F., Christie, R., MacManus, D. & Sheaf, C. (2021), ‘Non-axisymmetric aero-engine nacelle design by surrogate-based methods’, *Aerospace Science and Technology* **117**, 106890.
- Tejero, F., Goulos, I., MacManus, D. & Sheaf, C. (2020), Effects of Aircraft Integration on Compact Nacelle Aerodynamics, in ‘AIAA SciTech 2020 Forum and Exposition, AIAA Paper 2020-2225’.
- Tejero, F., MacManus, D., Matesanz-Garcia, J., Swarhout, A. & Sheaf, C. (2022), Towards the Design and Optimisation of Future Compact Aero-Engines: Intake/Fan Cowling Trade-Off Investigation, in ‘56th 3AF International Conference on Applied Aerodynamics, Paper FP04-AERO2022-Tejero’.
- Tejero, F., MacManus, D. & Sheaf, C. (2020), Impact of Droop and Scarf on the Aerodynamic Performance of Compact Aero-Engine Nacelles, in ‘AIAA SciTech 2020 Forum and Exposition, AIAA Paper 2020-1522’.
- Tejero, F., Robinson, M., MacManus, D. & Sheaf, C. (2019), ‘Multi-Objective Optimization of Short Nacelles for High Bypass Ratio Engines’, *Aerospace Science and Technology* **91**, 410–421.
- Tonda, A. (2019), ‘Inspyred: Bio-inspired algorithms in python’, *Genetic Programming and Evolvable Machines* **21**, 269–272.
- Vassberg, J. C. & et al. (2014), ‘Summary of the Fourth AIAA Computational Fluid Dynamics Drag Prediction Workshop’, *Journal of Aircraft* **51**(4), 1070 – 1089.
- Vassberg, J., Dehaan, M., Rivers, M. & Wahls, R. (2008), Development of a Common Research Model for Applied CFD Validation Studies, in ‘26th AIAA Applied Aerodynamics Conference, AIAA Paper 2008-6919’.

- Viswanath, A., Forrester, A. & Keane, A. (2011), 'Dimension Reduction for Aerodynamic Design Optimization', *AIAA Journal* **49**(6), 1256–1266.
- Xie, J., Huang, J., Song, L., Fu, J. & Lu, X. (2022), 'An Effort Saving Method to Establish Global Aerodynamic Model Using CFD', *International Journal of Numerical Methods for Heat & Fluid Flow* **94**(11), 1–19.
- Xue, R., Jiang, J. & Jackson, A. (2019), 'Effect of Bypass Ratio on Optimal Fan Outer Pressure Ratio and Performance for Turbofan Engines', *International Journal of Aeronautical and Space Sciences* **20**, 157–164.
- Zhang, X., Xie, F., Ji, T., Zhu, Z. & Zheng, Y. (2021), 'Multi-Fidelity Deep Neural Network Surrogate Model for Aerodynamic Shape Optimization', *Computer Methods in Applied Mechanics and Engineering* **373**.

